Correlations of intermediate mass fragments from Fe+Ta, Au, and Th collisions

T. C. Sangster,[1] M. Begemann-Blaich,[1,2] Th. Blaich,[1,3] H. C. Britt,[1] L. F. Hansen,[1] M. N. Namboodiri,[1] and G. Peilert[1,*]

[1] *Lawrence Livermore National Laboratory, Livermore, California 94550*
[2] *Gesellschaft für Schwerionenforschung, D-64220 Darmstadt, Germany*
[3] *Universität Mainz, D-55099 Mainz, Germany*

(Received 16 May 1994)

Charge, velocity, and angular correlations between intermediate mass fragments (IMF) are presented for 50 and 100 MeV/nucleon Fe bombardments of Ta, Au, and Th targets. Correlation functions generated as a function of the relative velocity and the opening angle between two IMF's are qualitatively independent of the projectile energy and target mass and show a suppression at small relative velocities and opening angles due to the Coulomb repulsion between the fragments. The correlations are consistent with IMF's emitted primarily from a highly excited target residue following a rapid preequilibrium cascade. The correlation data are compared to model calculations using the event generator MENEKA and the quantum molecular dynamics (QMD) code with a statistical deexcitation of residual fragments utilizing the multifragmentation code SMM. All data are consistent with a simultaneous multifragmentation at a freeze-out density of 0.1–0.3 times normal nuclear matter density or a more sequential emission with time constant $\tau \leq 500$ fm/c.

PACS number(s): 25.70.Pq

I. INTRODUCTION

A topic of great interest in nuclear physics is the onset of multifragmentation in heavy nuclei at moderate excitation energies and the possible relation of this experimental phenomenon to a phase transition analogous to the liquid-gas transition in condensed matter physics. Such a transition is expected in infinite nuclear matter, but the characteristics in a finite nuclear system remain unclear. Recent experiments [1–9] on the correlations between intermediate mass fragments (IMF's) are beginning to give insight (time scales, source sizes, etc.) into the decay mechanism for multifragment emission, and these results are in turn leading to improvements in the models used to interpret the data [5,10,11].

Modeling of reactions with center-of-mass bombarding energies of a few hundred MeV to a few GeV generally involves a preequilibrium stage described in the earliest approaches by an intranuclear cascade (INC) model [12,13] and more recently by molecular dynamic pictures such as the quantum molecular dynamics (QMD) model [14,15] or the quasiparticle dynamics (QPD) model [16,17]. An intermediate approach has involved the use of the Boltzmann Master Equation (BME) [18]. Following this preequilibrium or dynamical stage, there remains a distribution of nucleons and complex fragments which can themselves be highly excited. The excited fragments then undergo further statistical decay. This statistical decay process has been modeled in various codes as a sequential evaporation (e.g., GEMINI [19], GEM [20]), as an explosive simultaneous multifragmentation (e.g., SMM [21] or other models [22]), and as a dynamical multifragmentation [23].

From the systematics of heavy-ion reaction studies at low and medium energies, a qualitative picture of the main features of these reactions is beginning to emerge. It appears that for total center-of-mass energies up to about 5 GeV, a dominant feature for reactions involving either a large projectile or a large target is the formation of a heavy residue (mass of order 200) which can exhibit different decay modes depending on the total excitation energy available [24–28]. Comparisons of data with the models described above have begun to show a consistent picture of the reaction processes over the broad range of energies available in the target residue. For modest excitation energies (up to about 300 MeV), the relatively slow fission process is important in the residue decay [29–31]. For higher excitation energies (up to order of 1 GeV), a fast preequilibrium cascade results in a final target residue that is generally too light to fission [31,32]. At still higher excitation energy (above 1 GeV), a multifragmentation mechanism emerges and dominates the residue decay [27,33]. Recent QMD calculations suggest that with increasing bombarding energy a rapid compression-decompression mechanism emerges in the initial stage of the reaction and leads to a direct multifragmentation where a highly excited heavy residue is no longer formed with high probability [34,35].

An examination of recent Kr+Au data [35] suggests that the best region to search for thermally driven multifragmentation is in the 1–5 GeV total energy region covered by the experiments reported in this paper. In terms of IMF emission from the 1–5 GeV energy regime, the global character of the reactions has been explored by several groups with generally consistent results. Calculations with dynamical entrance channel models such as

*Present address: Am Kettnersbusch, 3D-51379, Leverkusen Opladen, Germany.

QMD [14,15,25] and QPD [16,17] tend to produce direct IMF's at rapidities close to that of the light projectile in asymmetric collisions, whereas the experiments measure large yields from the heavy-target system (or in the heavy-projectile system in experiments utilizing inverse kinematics).

A comprehensive calculation [25] has shown that the inclusive IMF data from the present Fe+Au reaction studies at $E/A = 50$ and 100 MeV are consistent with the existence of highly excited target residues (predicted in QMD) which when deexcited using a statistical multifragmentation approach [21] yield a good representation of the observed IMF distribution. Similar results are obtained at higher bombarding energies for peripheral collisions [36]. In addition, recent systematic measurements of IMF distributions using Au projectiles have suggested that the IMF's come from a band of excitations in the heavy residues ($E/A = 5-10$ MeV) and are relatively independent of the initial dynamics of the reaction [27,33].

Correlations in charge and velocity between two or more IMF's emitted from a heavy-residue source may be a key to understanding the multifragmentation mechanism. In particular, the final state Coulomb interaction between two charged particles places restrictions on the minimum relative velocity at which they are detected in the laboratory. The minimum relative velocity for two fragments emitted simultaneously is simply given by their mutual Coulomb repulsion. However, if the fragments are emitted sequentially with a long time delay, their mutual Coulomb repulsion is minimal and this "Coulomb hole" or suppression of small relative velocities disappears. Sequential models can be used to reproduce this behavior and to estimate the relative emission times for IMF's [1–9]. These approaches have indicated emission times of less than a few hundred fm/c in intermediate-energy heavy-ion reactions. Multifragmentation models such as SMM assume that a dynamic expansion has taken place and the fragments are emitted simultaneously from an extended freeze-out volume. In this case the character of the Coulomb hole is affected by the freeze-out volume rather than the time delay between fragment emissions.

In this paper we present comprehensive results on two fragment correlations for IMF's in the range $4 < Z \leq 53$ from reactions of Fe beams on targets of Ta, Au, and Th. A complete description of the experimental setup, inclusive IMF distributions, selected aspects of the IMF correlations, and results from fission deexcitations in peripheral collisions have been presented previously [25,30–32]. Brief versions of some selected correlation results have also been published [5,9,11]. In Sec. II we give a short overview of the experimental setup. In Sec. III we present the general properties of the two-fragment data set. Section IV gives the experimental systematics for the two-fragment correlation functions, and Sec. V contains the comparison of the data with the two very different models, MENEKA and QMD+SMM.

II. EXPERIMENTAL OVERVIEW

The experiment was performed using $E/A = 50$ and 100 MeV Fe beams from the LBL Bevalac accelerator and the PAGODA detector array [37]. The detector layout and an individual PAGODA module are shown schematically in Fig. 1. The eight modules are mounted symmetrically around a target chamber at polar angles of 36°, 72°, 108°, and 144° and subtend approximately 26° in both theta and phi for a total solid angle coverage slightly greater than 10% of 4π. Each module is a composite detector consisting of two position sensitive multiwire proportional counters (MWPC's), a low-pressure proportional counter (PC), a high-pressure, axial field ionization chamber (IC), and a nine-element fast-slow plastic phoswich array.

For fragments with $Z \geq 4$, velocities and positions are obtained using timing and position information from the two MWPC's. For each fragment, the charge (Z), spatial coordinates ($\theta_{\mathrm{lab}}, \phi$), and vector velocity ($\mathbf{v}$) are determined using dE/dx and time-of-flight (TOF) information as well as the local (X, Y) coordinates obtained from the MWPC's. These quantities can then be used to study correlations and generate correlation functions in various parameters for events containing two or more IMF's.

The charge resolution of the various identification masks for the IMF's ($2 \leq Z < 18$) is generally quite good: The overall IMF charge resolution for all events

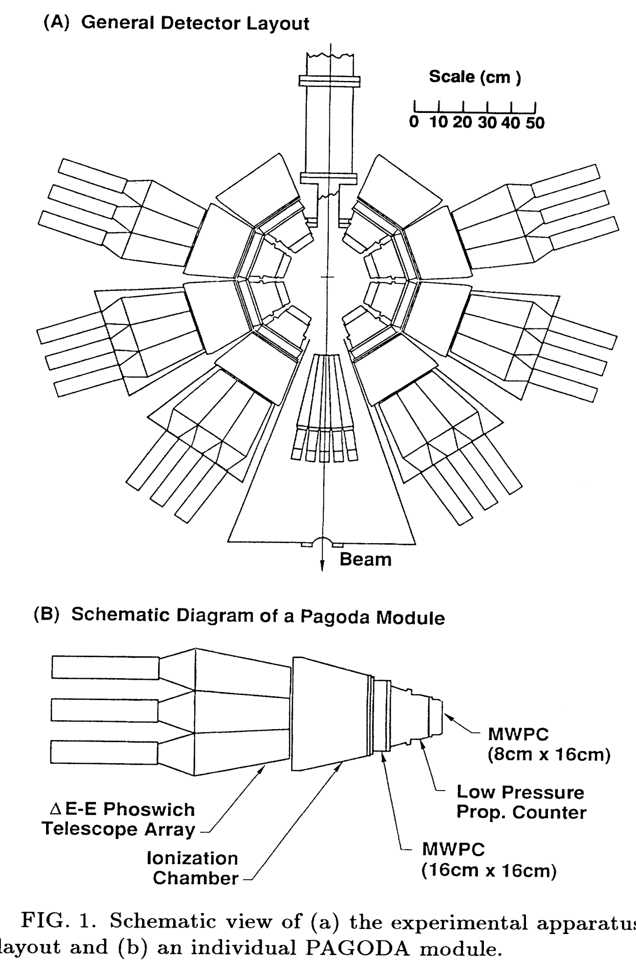

FIG. 1. Schematic view of (a) the experimental apparatus layout and (b) an individual PAGODA module.

is close to unity for $Z < 10$, approximately 2 units for fragments with $10 \leq Z \leq 20$, and 2–3 units for fragments in the fission-mass region. The velocity resolution of the original PC-TOF calibration is 0.05 cm/ns between 0.5 and 2.4 cm/ns ($E/A = 0.5 - 3.0$ MeV). Using the measured TOF, the velocity calibration has been extended to 4.1 cm/ns ($E/A = 8.8$ MeV) with comparable resolution.

All coincidence combinations of two fragments in the measured charge interval $5 \leq Z_{i,j} \leq 53$ and with individual fragment kinetic energies between 0.5 and 8.8 MeV per nucleon were identified for all systems. Binary fission pairs were identified and explicitly removed. Fission events were defined as two fragments on opposite sides of the beam with individual fragment charges and a charge sum greater than 16 and 46, respectively. No other event selection criteria were applied. Correlation functions, discussed in Sec. IV, were constructed following the formalism of Ref. [38] where the two-particle coincidence spectrum is divided by a suitably constructed background distribution which contains all the details of the experimental acceptance and reaction dynamics except those associated with the final state Coulomb interaction. Such a background spectrum is obtained using the technique of event mixing, first suggested by Kopylov [39], in which two fragments from different, but kinematically similar, events are treated as an actual pair of coincident fragments. Since only fragments from true coincidences are used to construct the mixed-event background and all constraints applied to the true pairs are also applied to the background pairs, the mixed distribution essentially reflects the two-fragment phase space population of the detector array in the absence of any final state interaction.

III. RESULTS: TWO-PARTICLE DISTRIBUTIONS

In this section we present the results for the charge, angular, and velocity distributions of the IMF's under the condition that a second IMF in a particular Z range is observed anywhere else in the array. Three representative charge intervals were used in the data sorting: L ($5 \leq Z \leq 12$), M ($12 < Z < 22$), and H ($22 \leq Z \leq 53$). Binary fission pairs have been excluded from this data sample.

Figure 2 shows angular distributions for fragments in the L, M, and H groups when the second detected fragment is in a particular Z group. The very striking feature seen here is that the angular distributions do not depend significantly on the charge of either fragment.

Similarly, Fig. 3 shows charge distributions for the first fragment when the second detected fragment is in a particular Z group. The plots show that the charge distributions are nearly identical when the second detected fragment is in the L or M group. For second fragments in the H group, the exclusion of fission events constrains the data to asymmetric pairs and the maximum charge for the first fragment allowed by the fission cut is 16. However, within the interval $5 \leq Z \leq 16$, the shape of the charge distribution at all laboratory angles is essentially independent of the charge of the coincident fragment.

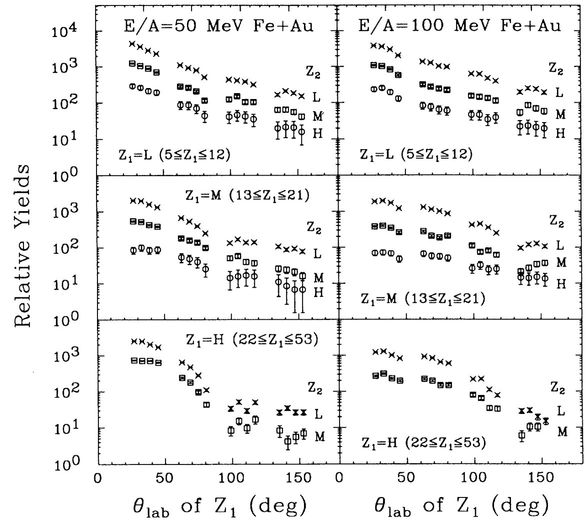

FIG. 2. Angular distribution in the laboratory frame for IMF Z_1 detected in coincidence with a second IMF, Z_2, for the reactions $E/A = 50$ and 100 MeV Fe+Au. The IMF's have been binned according to the charge intervals L ($5 \leq Z_2 \leq 12$), M ($12 < Z_2 < 22$), and H ($22 \leq Z_2 \leq 53$).

If the fragment velocity distributions are projected in a similar fashion, there is no apparent correlation between the velocities of the two fragments. Other quantities that can be projected from the two-fragment data set are the relative velocity ($\mathbf{v}_{\rm rel}$) of the two IMF's in their mutual reference system and the center-of-mass velocity of the fragment pair ($\mathbf{v}_{\rm pair}$) in the laboratory system. As vector quantities, these velocities completely define the kinematics of the two fragments. The magnitudes of $\mathbf{v}_{\rm rel}$ and $\mathbf{v}_{\rm pair}$ for the system $E/A = 100$ MeV Fe+Au are shown in

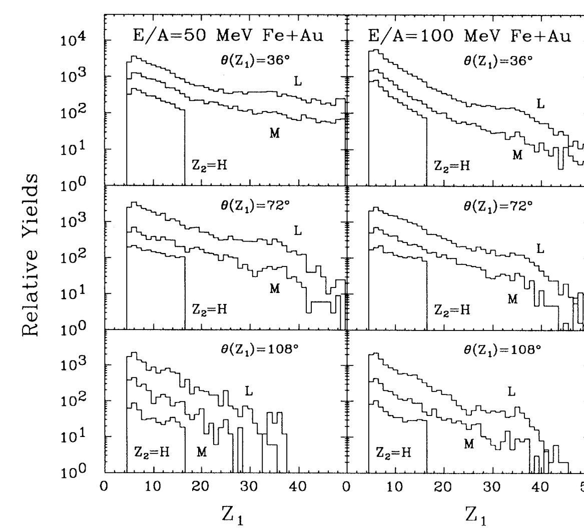

FIG. 3. Charge distribution for IMF's detected in a particular PAGODA module (laboratory angle) in coincidence with a second IMF in one of the charge intervals L, M, or H; data are from both the $E/A = 50$ and 100 MeV Fe+Au reactions.

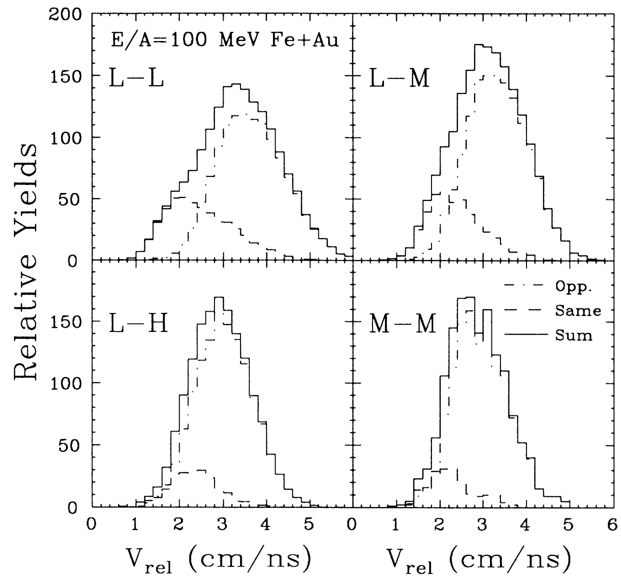

FIG. 4. Relative velocity distributions for various combinations of L, M, and H gates on two coincident IMF's from the system $E/A = 100$ MeV Fe+Au. The spectra are also shown separately for two IMF's emitted on the same side or on opposite sides of the beam.

Figs. 4 and 5 for all L, M, and H combinations. The $\mathbf{v}_{\rm rel}$ distributions show significant differences due to the acceptance for fragment pairs detected on the same side or on opposite sides of the beam (see Fig. 1), but the mean values and standard deviations of the distributions vary only slowly as a function of the Z cut and they are independent of the target and bombarding energy. Figure 6 shows the mean values of $\mathbf{v}_{\rm rel}$ and $\mathbf{v}_{\rm pair}$ as well as the charge asymmetry $|Z_1 - Z_2|$ plotted as a function of the Coulomb product $Z_1 Z_2$ for the system Fe+Au at both bombarding energies. The Coulomb product is a convenient dependent variable since it is directly proportional to the relative velocity. The shift of $v_{\rm pair}$ to smaller values with increasing bombarding energy reflects the expected shift in kinematics for a target residue source.

The lack of any gross correlations between kinematic and charge variables suggests that the charge and kinematic distributions of the emitted IMF's are independent of the target and bombarding energy. This result is consistent with the assumption that the observed IMF's are coming from the decay of a common target residue whose characteristics are also independent of the target and bombarding energy. As demonstrated earlier [25], the measured inclusive distributions for IMF's are not consistent with those expected from the early stages of the reaction as predicted by QMD. Furthermore, these results suggest that there is no strong correlation between the size of the residue source and the size of the emitted fragments.

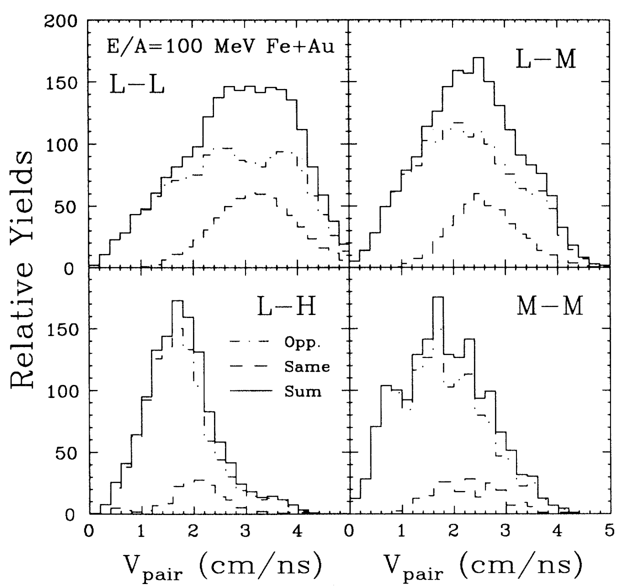

FIG. 5. Pair velocity distributions for various combinations of L, M, and H gates on the two coincident IMF's from the system $E/A = 100$ MeV Fe+Au. The spectra are also shown separately for two IMF's emitted on the same side or on opposite sides of the beam.

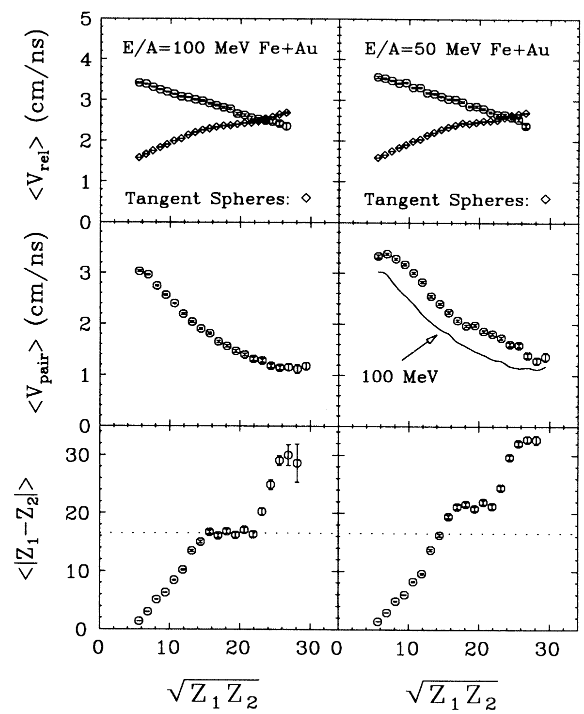

FIG. 6. Mean values for the charge difference, pair velocity, and relative velocity of coincident IMF's as a function of the Coulomb product $Z_1 Z_2$ for both the $E/A = 50$ and 100 MeV Fe+Au reactions. Diamonds in the upper panels show calculations of the mean velocities generated by Coulomb repulsion from two touching spheres with a radius parameter $r_0 = 1.4$ fm.

IV. TWO-PARTICLE CORRELATION FUNCTIONS

The correlation functions in relative angle and relative velocity between two emitted IMF's have been generated as described in Sec. II. The data were sorted into bins of the product Z_1Z_2 since the primary correlation being probed is the Coulomb final state interaction. In addition, the quantity $v_{\rm red} = v_{\rm rel}/(Z_1+Z_2)^{1/2}$ has been shown by Kim *et al.* [3] to allow a scaling of the data from different Z's over limited ranges. Therefore we have chosen to sort correlation functions for both $v_{\rm red}$ and $v_{\rm rel}$ as well as for the relative angle between the two fragments, $\theta_{\rm rel}$.

As described in Sec. II, these correlation functions were derived by taking ratios between distributions generated using correlated pairs (true) and pairs constructed by mixing two fragments from different physical, but kinematically similar, events (background), effectively eliminating acceptance basis. Deviations from unity in this ratio are indicative of final state correlations such as Coulomb repulsion. In all cases the true and background distributions were developed separately for two classes of events: (1) two IMF's detected on opposite sides of the beam and (2) two IMF's detected on the same side of the beam. In the regions where these two correlations overlap in relative velocity or angle, it was found that the correlations obtained from the two classes were effectively identical. Therefore the distributions (true and background) for the two acceptance classes have been combined into single spectra before taking the ratio to form the correla-

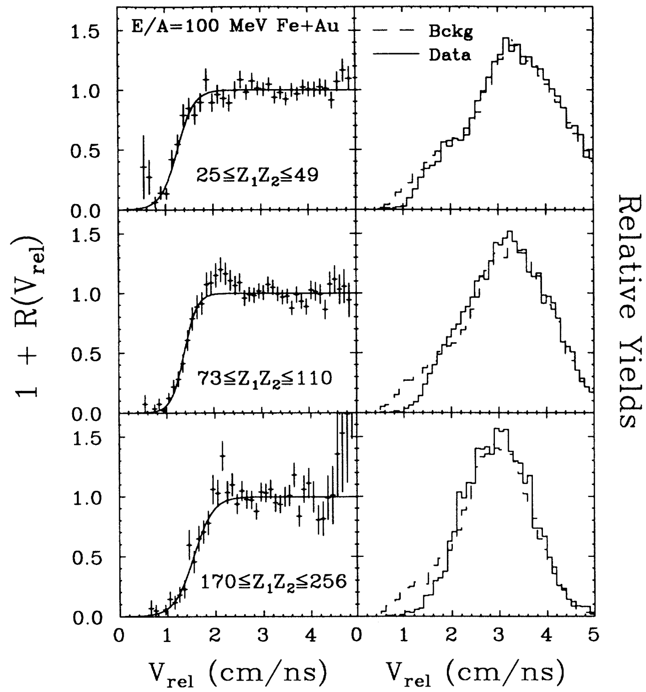

FIG. 8. Relative velocity correlation functions (left side) plus coincidence and background spectra (right side) for various gates on the Coulomb product Z_1Z_2; data are from the $E/A = 100$ MeV Fe+Au reaction.

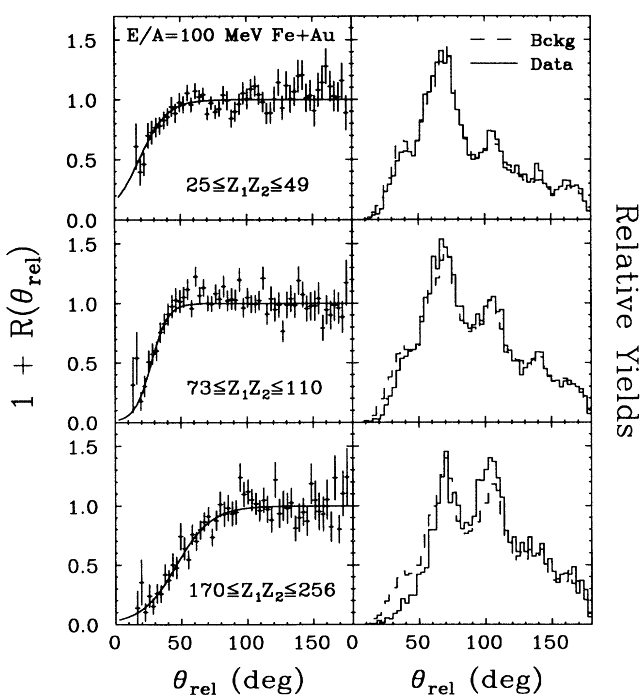

FIG. 7. Relative angle correlation functions (left side) plus coincidence and background spectra (right side) for various gates on the Coulomb product Z_1Z_2; data are from the $E/A = 100$ MeV Fe+Au reaction.

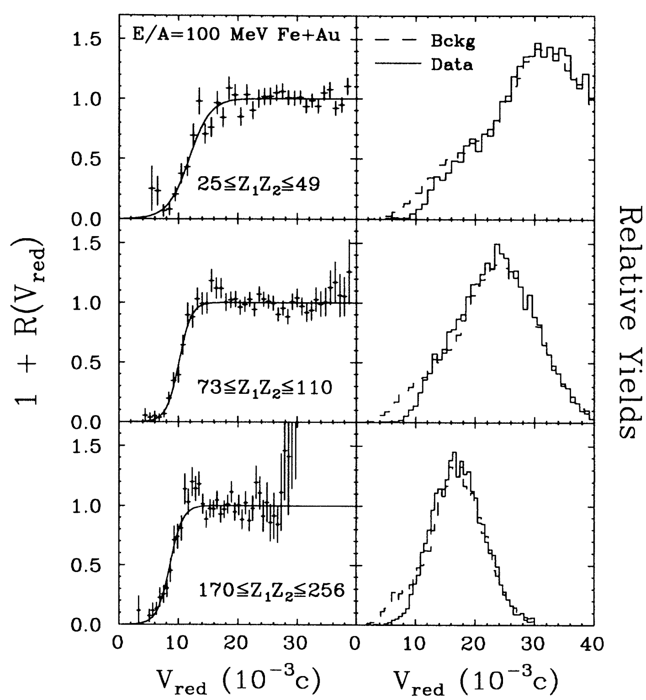

FIG. 9. Reduced velocity correlation functions (left side) plus coincidence and background spectra (right side) for various gates on the Coulomb product Z_1Z_2; data are from the $E/A = 100$ MeV Fe+Au reaction.

tion functions. In the analysis the $E/A = 100$ MeV data were divided into six Z_1Z_2 bins, while the $E/A = 50$ MeV data were sorted into five.

Figures 7–9 show examples of the raw correlation data for true (coincident pairs) and background (mixed-event pairs) distributions and their ratios for the reaction $E/A = 100$ MeV Fe+Au and three representative Z_1Z_2 cuts. The structure in the angular distributions reflects the acceptance of the PAGODA detector. The true and background data are normalized to the same total number of events. The correlation functions show very distinctly the expected "Coulomb hole" at small relative velocity and angle. The correlation functions approach unity at angles or velocities outside of the Coulomb hole region as they should if Coulomb repulsion is the only major final state correlation contained in the data and if the background distribution is constructed properly. We should note that nonconservation of momentum in the mixed-event background can distort the asymptotic behavior of the correlation functions. This leads to a correlation function which continues to rise with increasing relative (or reduced) velocity. Because of the planar nature of the PAGODA detector and the treatment of the mixed-event background (distinction between same and opposite side pairs), this distortion is minimal in the correlation functions shown in Figs. 7–12.

Figures 10–12 show composites of the correlation function data for the $E/A = 50$ and 100 MeV Fe+Au reactions and all cuts. The main qualitative feature is the increase in the width of the Coulomb hole with increas-

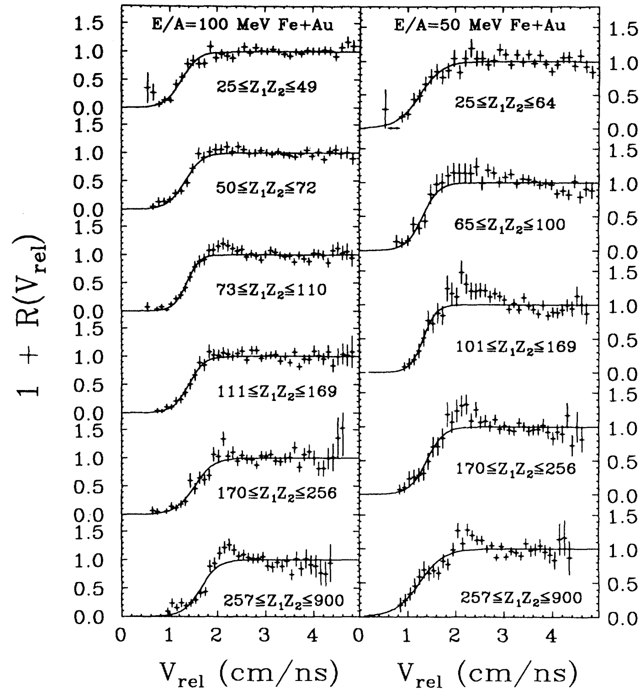

FIG. 11. Relative velocity correlation functions for all gates on the Coulomb product Z_1Z_2; data are from both the $E/A = 50$ and 100 MeV Fe+Au reactions.

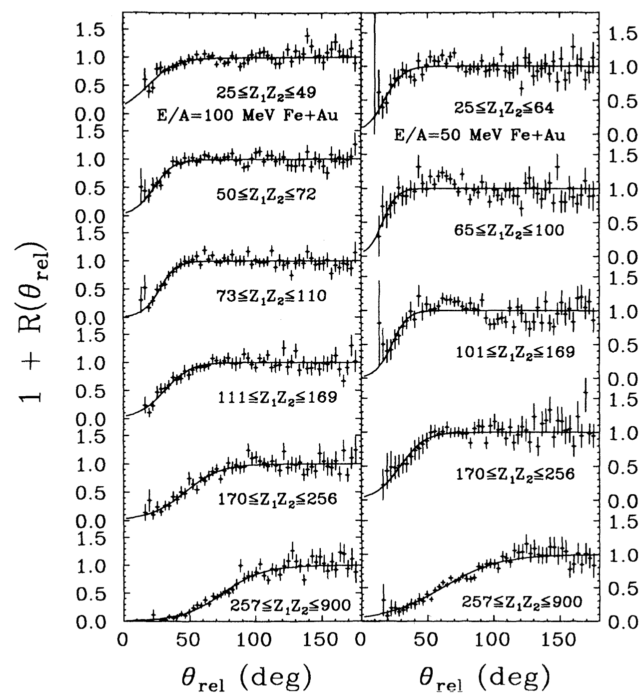

FIG. 10. Angular correlation functions for all gates on the Coulomb product Z_1Z_2; data are from both the $E/A = 50$ and 100 MeV Fe+Au reactions.

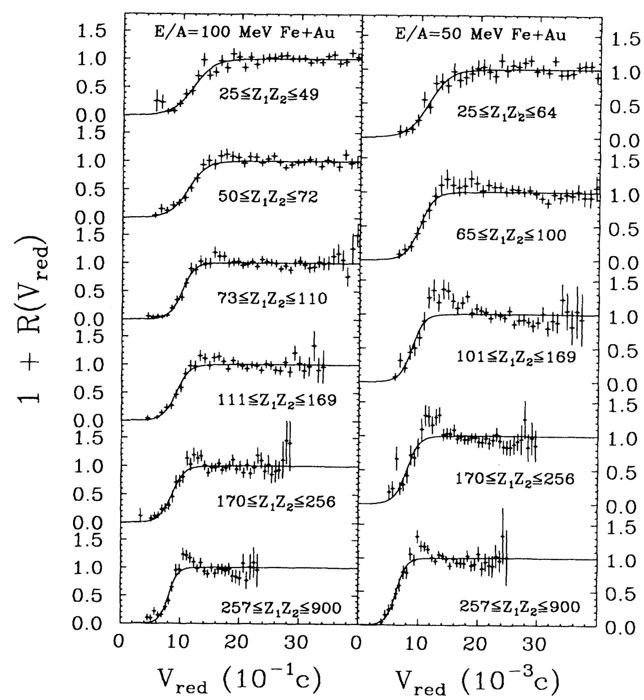

FIG. 12. Reduced velocity correlation functions for all gates on the Coulomb product Z_1Z_2; data are from both the $E/A = 50$ and 100 MeV Fe+Au reactions.

ing Z_1Z_2, reflecting the increasing Coulomb force. The quantity $v_{\rm red}$ does not serve as a good scaling parameter for combining data over our very large measured Z range, but it is useful for model comparisons (Sec. V) over the more limited intervals contained within a single Z_1Z_2 bin. A particularly interesting property of the data which shows up most clearly in the higher Coulomb product bins for the $E/A = 100$ MeV data is an apparent positive peak in the correlation function for relative velocities of approximately 2 cm/ns. The significance of this peak will be discussed in more detail in the following section.

In order to compare the large volume of data, the correlation functions have been empirically fit with a simple Fermi function:

$$f(x) = \frac{a}{1 + e^{(b-x)/c}}. \quad (1)$$

The half-depth points $f(x_{1/2} = b) = a/2$ can be used as a convenient fiducial for comparing correlation functions from different Z_1Z_2 cuts and for different reactions.

In Fig. 13 we show the systematics for the Coulomb hole half-depth points ($x_{1/2} = b$) for both the relative and reduced velocity correlation functions and the Fe beam reaction on all three targets (Ta, Au, and Th) at both energies ($E/A = 50$ and 100 MeV). As a reference, we show values from a simple two-touching-sphere distribution with radius parameter $r_0 = 1.4$ fm, calculated on an

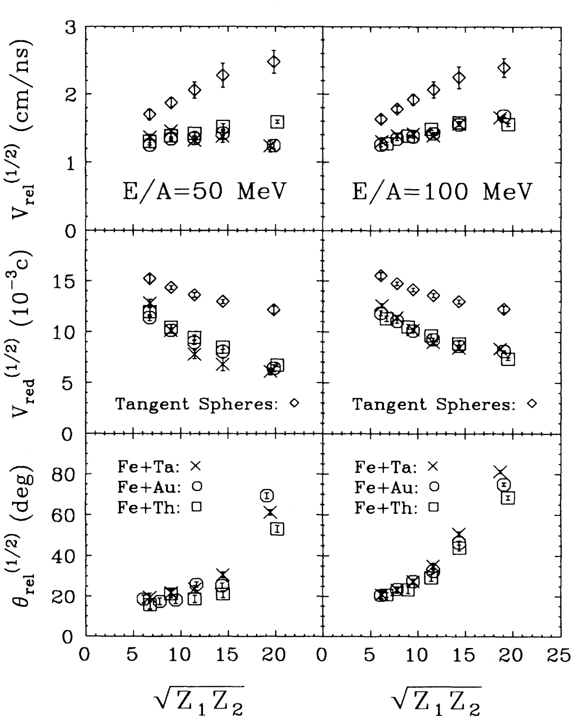

FIG. 13. Systematics for the half widths of the Coulomb holes in the correlation functions for relative angle, reduced velocity, and relative velocity. Diamonds show calculations of the velocities generated by Coulomb repulsion from two touching spheres with a radius parameter $r_0 = 1.4$ fm; data are from both the $E/A = 50$ and 100 MeV Fe+Au reactions.

event-by-event basis using the measured (Z_1, Z_2) pairs in a given Z_1Z_2 bin. The mean values of the measured $v_{\rm rel}$ distributions for the gold target were shown previously in Fig. 6. The most striking feature of the velocity spectra is the similarity for different targets and energies. At the highest values of Z_1Z_2, the average measured relative velocities smoothly approach the values seen for fission decay which were published previously and agree with global fission systematics [30].

Figure 13 also shows the Coulomb hole systematics for the relative opening angle distributions. For the largest Z_1Z_2 cuts, there is a small target dependence with the heavier targets showing the smallest $\theta_{1/2}$ values. This dependence is consistent with a larger residue source for the heavier targets. The larger source would give a slightly stronger Coulomb kick to the observed IMF pair, reducing the final opening angle (i.e., $v_{\rm pair}$ increases, while $v_{\rm rel}$ remains constant). At $E/A = 50$ MeV, the Coulomb holes becomes less distinct in the lower Z_1Z_2 bins, but the results are qualitatively similar. These results tend to confirm the identification of the relative velocity as the most relevant variable for studies of the Coulomb hole systematics.

When considering the emission of fragments, it is instructive to look for the existence of a preferred emission orientation in the two-fragment system. A preference for longitudinal emission may indicate a more timelike (sequential) than spacelike (simultaneous) emission pattern which would suggest a finite emission time. In Fig. 14, we show the longitudinal ($v_{\rm par}$) and transverse ($v_{\rm per}$) components of the relative velocity projected onto the pair velocity for the Coulomb product constraint $Z_1Z_2 < 200$ and the system $E/A = 100$ MeV Fe+Au. Figure 14(a) shows the correlated projections, while Fig. 14(b) shows the mixed-event background. The effect of the final state Coulomb interaction is clearly visible at small values of $v_{\rm per}$ and $v_{\rm par}$. Figures 14(c) and 14(d) show the two-dimensional correlation function obtained from the ratio of the two distributions in Figs. 14(a) and 14(b) as a contour and lego plot, respectively. There is clearly a symmetric Coulomb hole showing no preference for longitudinal or transverse emission and the expected broad, featureless plateau at larger values of $v_{\rm per}$. Figure 15 shows the same set of results for the $E/A = 50$ MeV Fe+Au system.

The question of a preferred orientation between the vectors $\mathbf{v}_{\rm rel}$ and $\mathbf{v}_{\rm pair}$ can also be investigated by looking at the correlation in the angle between them, ψ. Figure 16 shows this correlation for three different constraints on the opening angle $\theta_{\rm rel}$. The results show that there is no preferred direction for $\mathbf{v}_{\rm rel}$ relative to $\mathbf{v}_{\rm pair}$ for opening angles greater than 40°, which represents the majority of the data. For opening angles less than 40°, there is a distinct favoring of longitudinal emission, but this result is likely forced by the geometry of the emission process and the short emission time scale—because of Coulomb repulsion, two fragments end up with a small relative angle only if they are emitted more longitudinally (or sequentially).

In addition to the unconstrained correlations between two IMF's discussed above, it is also possible to develop

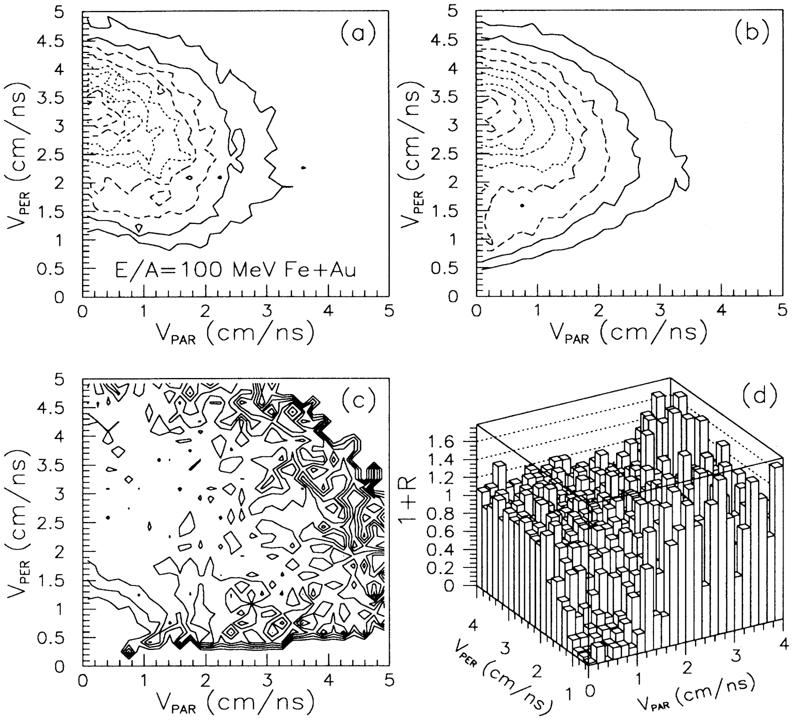

FIG. 14. Plots of the longitudinal versus transverse components of the relative velocity projected onto the pair velocity for the Coulomb product constraint $Z_1 Z_2 < 200$ and the system $E/A = 100$ MeV Fe+Au. Panel (a) shows the correlated and panel (b) shows the background distributions; (c) and (d) show the two-dimensional correlation functions as both a contour and lego plot, respectively [these are simply the appropriately normalized ratio of (a) and (b)]. A symmetric Coulomb hole is clearly visible, indicating little preference for either longitudinal (timelike) or transverse (spacelike) emission.

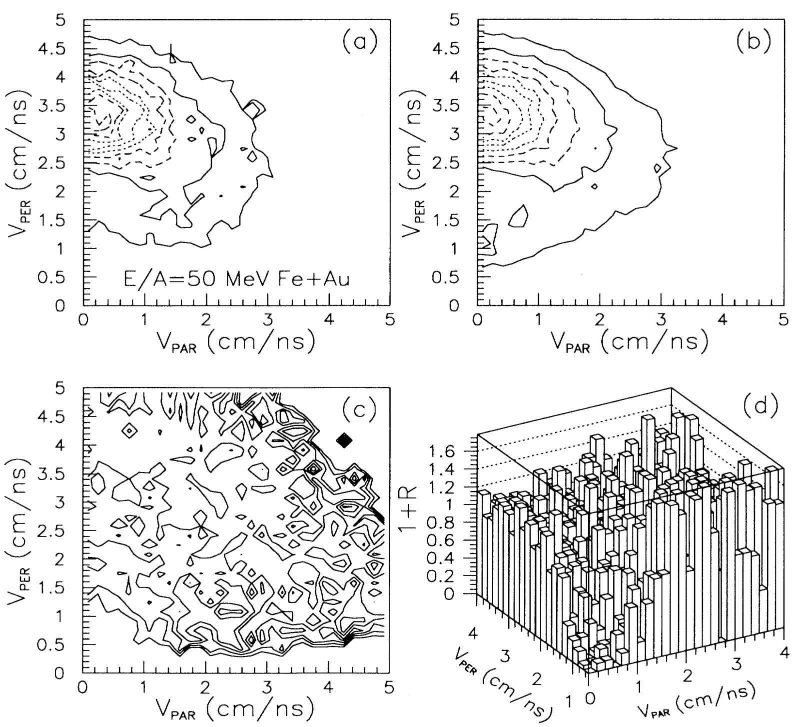

FIG. 15. Same as Fig. 14 except for the system $E/A = 50$ MeV Fe+Au.

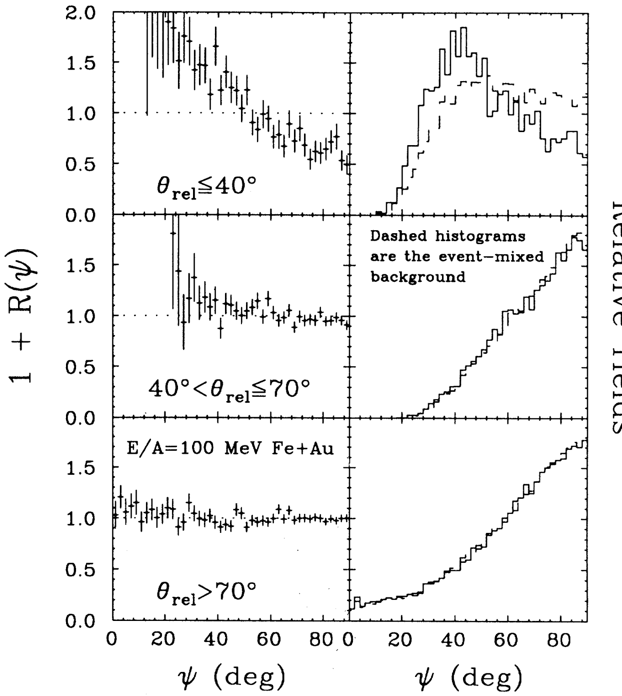

FIG. 16. Correlation in the angle between the relative and pair velocities, ψ, for various constraints on the relative angle; data are from the $E/A = 100$ MeV Fe+Au reaction.

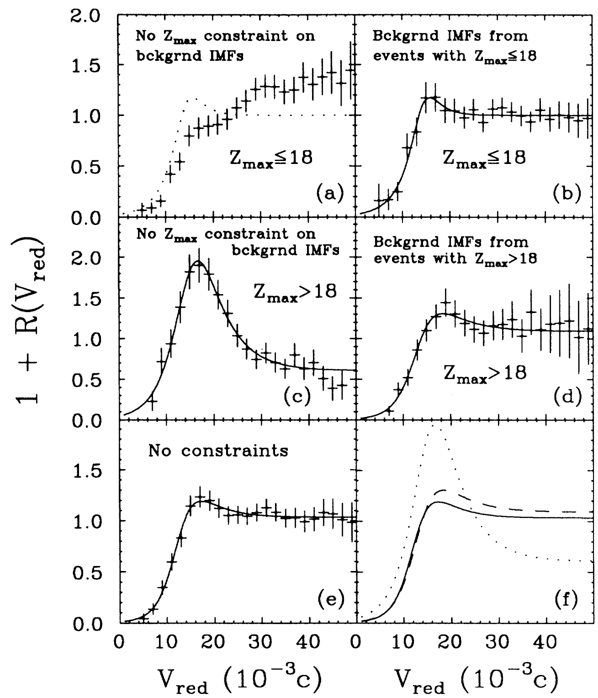

FIG. 17. Velocity correlations for the two lightest fragments in events where three IMF's are detected. The three-fragment data from all three $E/A = 100$ MeV systems have been summed together. Results are shown for various constraints on the charge of the heaviest fragment, $Z_{\max}$. The dotted curve in (a) is the fitted line from (b); the three curves in (f) are the fitted lines from (c), (d), and (e). See the text for further details.

correlation functions which are constrained by other properties of the observed event. The most instructive of these constraints is placed on the largest observed fragment charge $Z_{\max}$ in events containing three detected fragments. Figure 17 shows v_{red} correlation functions generated for the two lighter fragments for $Z_{\max} \leq 18$ and $Z_{\max} > 18$ with and without similar constraints on the background distribution. If the background constraints are the same as those in the true distribution, then, as expected, the correlation functions look very similar to the unconstrained correlation functions. However, if the background is unconstrained, then a new final state correlation is observed: For cases where the third fragment is heavy, a pronounced peak appears in the correlation function at $v_{\text{red}} \approx 20$. This peak represents the additional Coulomb repulsion on the IMF pair by the large third body. Since the acceptance in this experiment is approximately 10%, we miss most of the fragments in any given event. Therefore we would expect to see this third-body effect in the unconstrained two-particle correlation functions if there were a significant probability for an additional undetected large fragment in these reactions. The data show a small tendency in this direction for some Z_1Z_2 bins (see Figs. 10–12), but nothing of the magnitude seen in Fig. 17. This will be discussed further in the following section since the two models studied also show such a correlation.

V. MODEL COMPARISONS

The experimental two-fragment correlation data presented in the preceding sections and previous comparisons of the IMF inclusive data to the QMD+SMM model [25] support the qualitative conclusion that in this energy range the IMF's are coming primarily from the deexcitation of a heavy-target-like residue that remains following an initial preequilibrium cascade. Furthermore, it is clear that the observed Coulomb holes in the relative velocity distributions contain information on the time scale and freeze-out volume for IMF emission and that this information is important in determining the nature of the multifragmentation process. However, in order to use the correlation results to quantitatively determine IMF emission time scales and freeze-out volumes, it is necessary to realistically model the entire reaction process from the initial heavy-ion collision to the final multifragmentation stage. Various models have been proposed and developed which treat in a reasonable way one or another of the reaction stages, but at present there does not exist a truly comprehensive model. It is beyond the scope of the present predominantly experimental activity to develop a new, more comprehensive model, and there are currently new directions being pursued by several theoretical groups. We do, however, believe that the current data set is unique in its broad IMF acceptance (charge, velocity, and laboratory angle) and should be useful for testing future models. In order to get a qualitative estimate of the sensitivity of these correlations to the physics of the collision and the decay processes, in the next two subsections we make comparisons to two very different models, MENEKA and QMD+SMM.

The MENEKA model [40] is a simple three-body Coulomb trajectory calculation which has been applied in the spirit of a multifragmenting single moving source. It emits the two IMF's sequentially with a time scale that can be varied, and thus it can be used to make qualitative estimates of the IMF emission time scale. The QMD+SMM approach contains the dynamics of the original collision and the multiparticle Coulomb trajectories for the IMF's, but it assumes a simultaneous breakup. It does, however, allow for a variable freezeout volume.

A. MENEKA comparisons

The MENEKA code [40] provides a framework within which the trajectories of two sequentially emitted IMF's can be followed taking into account the mutual Coulomb repulsion of three bodies (2 IMF's + residual source) and the recoil effects of the residual source. The essential features of the code are isotropic surface emission from a spherical, compound source characterized by a unique radius with angular momenta chosen randomly from a triangular distribution limited by the condition $I_{\max} = \mathbf{p} \times \mathbf{R}$. The emission energies are selected to reproduce the experimentally measured distributions, and the distribution of time delays between fragment emission is given by $e^{-t/\tau}$.

The version of the code used for this analysis requires input for the properties of the emitted IMF's (two charges and masses as well as the corresponding kinetic energy distributions) and the source (charge, mass, radius, and linear momentum). It also requires as input the emission time constant τ. These inputs were fixed independently for each Z_1Z_2 interval used in sorting the experimental data. A radius parameter $r_0 = 1.4$ was used for all fragments and sources. For each Coulomb product bin, the two input charges were approximated by the measured mean charges of the lighter and of the heavier fragment. The corresponding kinetic energy distributions for the lighter and heavier fragments were used in the code initialization to establish the effective temperatures and emission barriers. For $\tau = 100$ fm/c, the linear momentum of the source was adjusted to give the best overall representation of the inclusive data which is shown in Fig. 18 for one of the Z_1Z_2 cuts. The MENEKA data shown in Fig. 18 have been passed through the PAGODA acceptance filter and are compared to the experimental distributions for the $E/A = 100$ MeV Fe+Au reaction (note that the MENEKA distributions shown in Fig. 18 are essentially independent of τ). The comparison in Fig. 18 shows that MENEKA does quite well at reproducing both the inclusive distributions (momentum and angular distributions) and some two-particle distributions (relative velocity and angle). However, there is a qualitative difference in the pair velocity which is uniformly lower and more sharply peaked than the data. The origin of this deviation could come from either or both of two unrealistic assumptions inherent to the code. First, MENEKA always produces a three-body final state which contains a large undetected fragment. As discussed in the previous section, the data do not seem to be consistent with such a final state. Second, for each event MENEKA produces a single moving source with no thermal expansion, whereas the data presumably come from a superposition of hot sources with a spectrum of masses and velocities. Nevertheless, we believe that MENEKA can still be used to give a qualitative estimate of the multifragmentation time scale.

With the parametrization discussed above, $v_{\rm red}$ and $\theta_{\rm rel}$ correlation functions were constructed for emission lifetimes of 50, 100, 250, 500, and 1000 fm/c by treating the detector-accepted MENEKA pairs exactly like the data. Figures 19 and 20 show comparisons between calculated and measured correlation functions for two Z_1Z_2 cuts on the $E/A = 50$ and 100 MeV Fe+Au data. From these results it is possible to conclude that the data are consistent with an emission lifetime of less than 500 fm/c, but the limited statistical accuracy of the data and the simplicity of the model do not allow us to set a more stringent limit. Figures 19 and 20 also indicate that the correlation functions generated using MENEKA are not very sensitive to the emission time for lifetimes less than 250 fm/c.

Although this estimate is consistent with previously re-

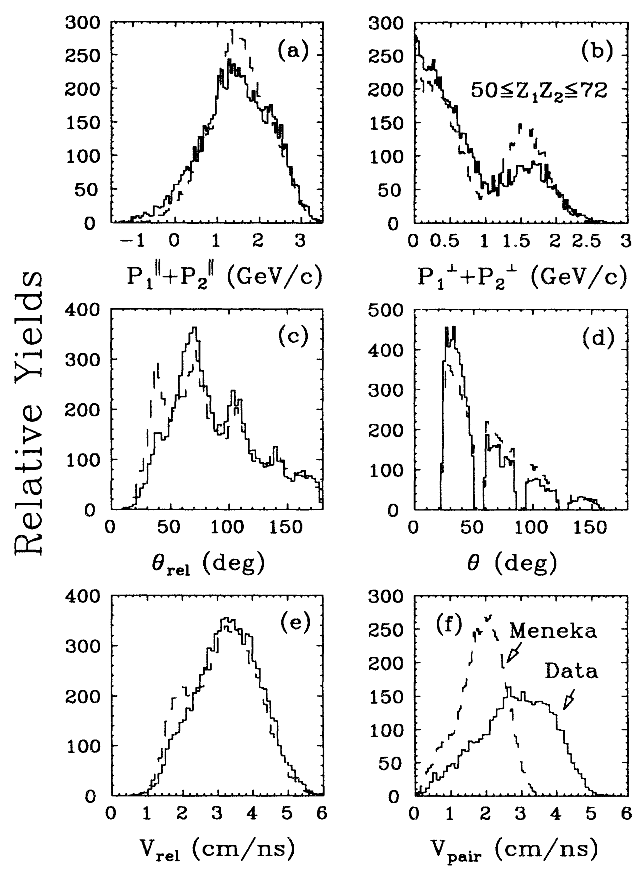

FIG. 18. Comparisons between the data ($E/A = 100$ MeV Fe+Au) and MENEKA calculations for velocity, angular, and momentum distributions.

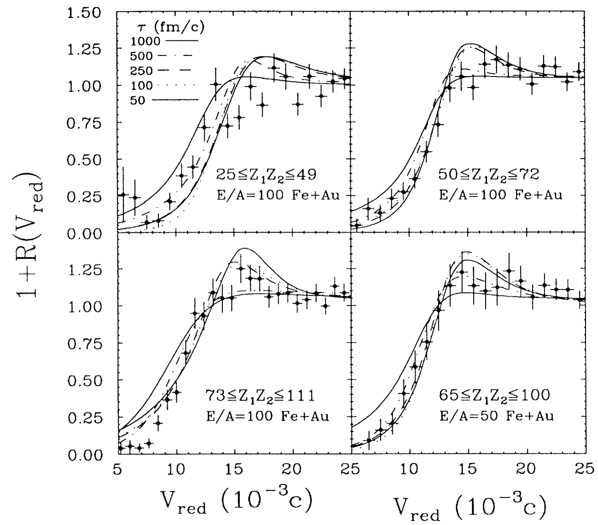

FIG. 19. Calculated reduced velocity correlation functions from MENEKA for various values of the emission lifetime τ and various constraints on the Coulomb product Z_1Z_2. The symbols are the experimental results.

ported lifetime limits between 100 and 200 fm/c [3,4,6,7], it appears that the present analysis does not achieve the same sensitivity to short emission times for similar reactions even though, in one instance [7], the same code (MENEKA) was used. This apparent lack of sensitivity and longer emission time appear to be real effects caused by the much lower fragment kinetic energy detection thresholds ($E/A = 0.5$ MeV versus several MeV per nucleon for the light fragment data in [3,4,7]) and the much broader polar angle coverage of the PAGODA detector. In Ref. [3] it was shown that selecting higher-velocity fragment pairs decreases the apparent emission time. Indeed, the data in [3,4,7] are limited to polar angles less than $35° - 40°$ where contamination from projectilelike fragments occurs (the inclusive energy spectra are shown in [3]). Since the low-energy detection threshold and broad angular acceptance of the PAGODA detector assure that the majority of the fragment pairs used in the present analysis comes from the decay of a single large residue source, it is perhaps not surprising that the emission times scale appears to be somewhat longer than 100–200 fm/c.

In addition, the discrepancy with the MENEKA results in Ref. [7] can be partially traced to differences (improvements) in the code itself. For example, our inputs were mean charges and kinetic energy distributions, whereas later versions of the code [7] used measured charge distributions and the kinetic energy spectra for each individual Z. The more realistic fragment input has been credited with significantly improving the time scale resolution [41] via correlation function comparisons. Our early work with MENEKA [5] represented the first application of this code for the extraction of fragment emission time scales. Since we are actually probing the limit at which the source geometry and the notion of an emission time scale become indistinguishable, in the next subsection we will address the fragment emission process from the other extreme: simultaneous emission from a variable density source.

One final relevant aspect of the MENEKA calculations is the enhancement in the v_{red} correlation functions at the edge of the Coulomb hole. The enhancement appears to be more sensitive to the time scale (virtually disappearing for $\tau = 1000$ fm/c) than the width of the Coulomb hole. As discussed above, this enhancement may be a signature for the presence of a heavy fragment in the final state. By construction, a large third fragment is always present in the MENEKA events. This issue will also be discussed further in the next subsection.

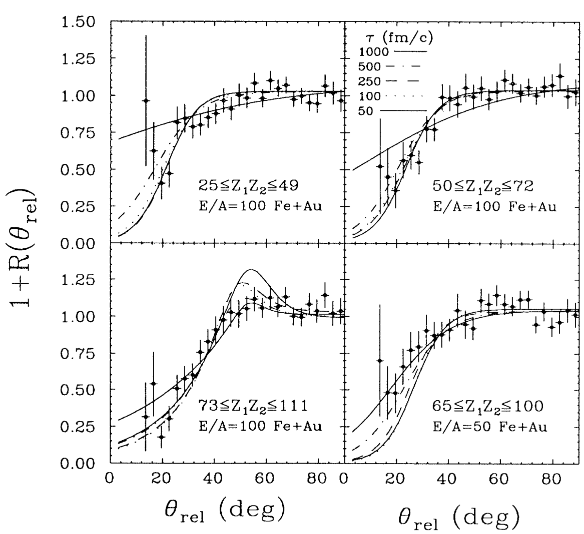

FIG. 20. Calculated relative angle correlation functions from MENEKA for various values of the emission lifetime τ and various constraints on the Coulomb product Z_1Z_2. The symbols are the experimental results.

B. QMD+SMM comparisons

The QMD model provides a microscopic dynamical calculation of a heavy-ion reaction. The version of the QMD model used in these calculations has been described previously and compared to IMF inclusive distributions from this experiment [25]. The model uses a local two- and three-body Skyrme interaction as well as a Coulomb and Yukawa interaction. For infinite nuclear matter, the Skyrme part of the interaction can be considered as a density-dependent interaction. The parameters of the interactions are adjusted to reproduce the properties of infinite nuclear matter, as well as the binding energy and radii of nuclei in the mass region $A = 2 - 200$. Furthermore, a Pauli potential [34] has been incorporated that simulates the Fermi aspects of the nucleon distributions [42]. The implementation of the Pauli potential into the dynamical QMD model yields two major improvements relative to earlier models. First, the ground states are now well defined, which yields much more stable initialized nuclei. Second, the excitation energy of the resulting fragments can be determined with respect to the true ground state and used to describe the long-term behavior (evaporation, multifragmentation, or fission) of those fragments in an independent model.

Previous investigations with the QMD model have shown [42] that there are two different mechanisms leading to multifragmentation. One is related to the mechanical rupture of the system whenever compressional degrees of freedom are important. The other mechanism produces fragments thermally from an equilibrated source. This thermal multifragmentation has so far not been described in a microscopic model like QMD [42]. Comparison of QMD to inclusive IMF data from this experiment [25] and exclusive IMF data at higher energies [35,36] have shown that a two-step model is necessary to reproduce the experimental data in this thermal expansion regime. This two-step model involves the calculation of initial kinematics and excitation energy of the target residue with QMD and a subsequent deexcitation plus Coulomb trajectory calculation utilizing the statistical multifragmentation model (SMM) of Botvina *et al.* [21].

Input for the SMM stage of the reaction is the mass and excitation energy of the fragments produced in QMD (more than one fragment or residue can be deexcited within the SMM simultaneously; care is taken to preserve the spatial coordinates of the resulting fragmentation products for the final Coulomb trajectory calculation). These values are consistently determined within the QMD approach. The only variable parameter, κ, in the SMM calculations is used to define the density or volume, $v = v_0(1+\kappa)$, of the freeze-out state when the fragments are created (v_0 is the normal ground state volume). Comparisons to inclusive data from this experiment [25] showed that the results were rather insensitive to this parameter; therefore, the calculations shown in Ref. [25] were made with a default value of $\kappa = 2$.

In the QMD+SMM calculation, all final state correlations are maintained and the properties of the excited target residues are determined on an event-by-event basis. The Hamilton equations of all nucleons are integrated, which implies that correlations between all the existing nucleons and fragments are treated in all orders. This is especially important if one deals with many IMF's which are influenced by a large number of lighter fragments and protons.

Comparisons to the experimental data can be carried out with κ treated as a variable parameter to study the volume dependence of the correlation functions for the extreme case of simultaneous IMF emission. In the following we compare results from this model for values of κ from 1 to 15 to the $E/A = 100$ MeV Fe+Au data. The theoretical calculations have been filtered to match the acceptance of the experiment and the correlations calculated with the same event-mixing technique.

In all cases the QMD calculation has been stopped after 300 fm/c and the excited fragments at that time used as input to the SMM. It has been shown that the mass and excitation energies of the IMF's do not depend sensitively on the time at which the transition is made as long as it is sufficiently beyond the end of the initial fast cascade [43]. Calculations for our reaction show that varying the switching time within the range of 100–300 fm/c does not affect the shape of the correlation functions.

A comparison of inclusive quantities calculated with a volume parameter $\kappa = 5$ is shown in Fig. 21. In this model there are no adjustable kinematic parameters and it is seen that for most quantities the model does quite well. The parallel momentum transfer is predicted to be somewhat high, which results in a more forward peaked angular distribution, but the relative velocity distribution is very close to the data and this is the fundamental quantity in all the two fragment correlations. The major deviation is in the pair velocity, which is lower and more sharply peaked in the model than in the data. In fact, the $v_{\rm pair}$ distribution from QMD+SMM is very close to that calculated with MENEKA and distinctly different from the data. That this difference persists to QMD+SMM even though this model has more realistic kinematics and a true multifragmentation is very surprising.

In Fig. 22, calculations of correlation functions for three Z_1Z_2 bins are shown as a function of κ and compared with the $E/A = 100$ MeV Fe+Au data. Two effects are evident from these comparisons. First, the Coulomb hole over this Z_1Z_2 range cannot be reproduced by a single value of κ. Lighter fragment pairs are most consistent with the smaller κ values (or, similarly, shorter

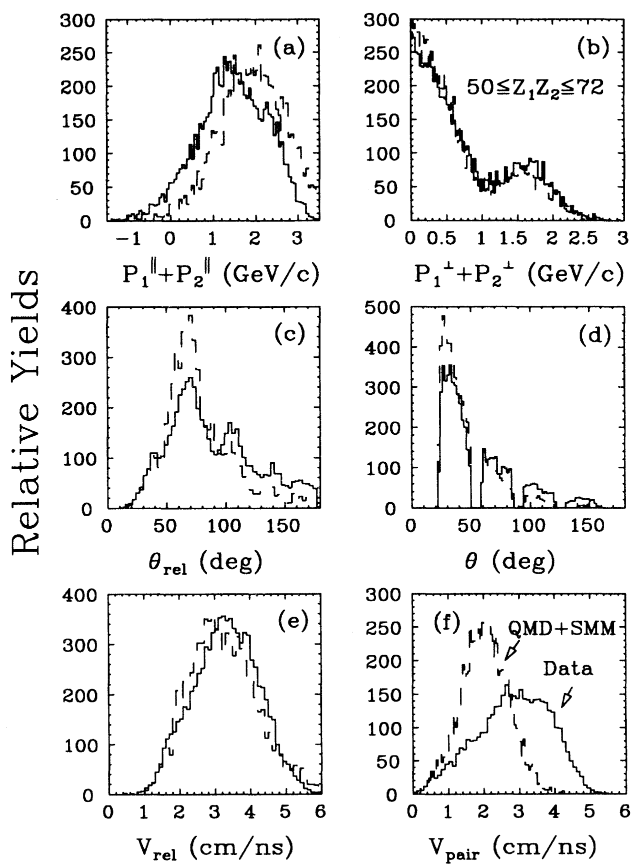

FIG. 21. Comparisons between the data ($E/A = 100$ MeV Fe+Au) and QMD+SMM calculations for velocity, angular, and momentum distributions.

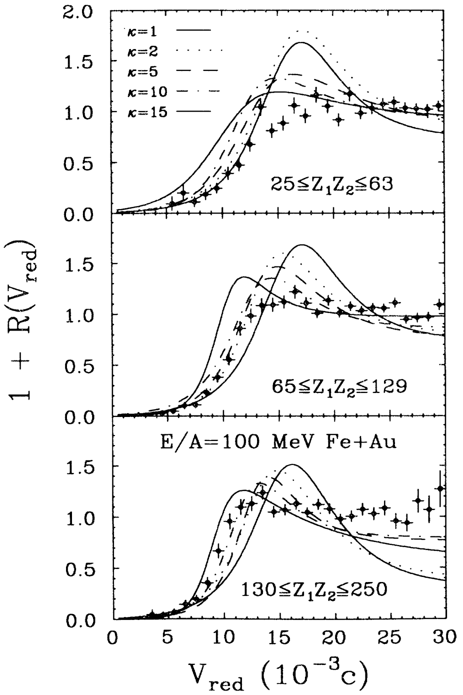

FIG. 22. Calculated reduced velocity correlation functions from QMD+SMM for various values of the volume parameter κ and various constraints on the Coulomb product Z_1Z_2. The symbols are the experimental results.

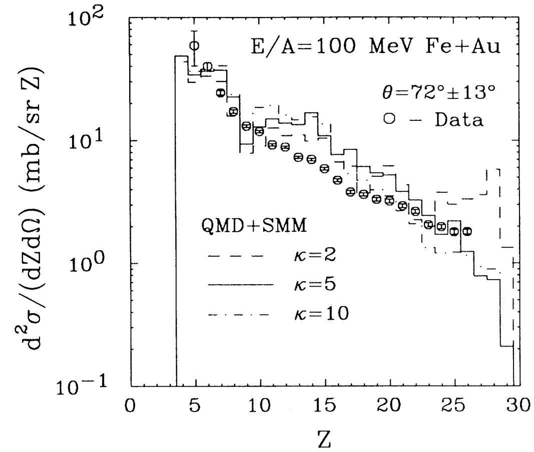

FIG. 23. Calculated charge distributions from the QMD+SMM model compared with the experimental two-fragment data (E/A = 100 MeV Fe+Au) for the constraint that at least two IMF's from QMD+SMM are accepted in the PAGODA detector filter.

emission times), while for the heavier pairs the data are more consistent with a value of κ closer to 10. Second, the calculations show a much greater positive enhancement at the edge of the Coulomb hole than is apparent in the data, especially for smaller Z_1Z_2. Although the comparison with the data does not yield a single best value for κ, the QMD+SMM model, which probes the extreme case of simultaneous multifragment emission, does reproduce the measured correlation functions with values of κ between 2 and 10 indicating a freeze-out volume of 3–10 times that of the ground state. This volume is entirely consistent with the emission time scale ($\tau \leq 500$ fm/c) determined with MENEKA.

For QMD, the overshoot or enhancement in the calculated velocity correlation functions is quite similar to what is seen in the MENEKA calculations. However, the data only show a pronounced overshoot if the additional constraint of an observed large remnant fragment is imposed as shown above and in [11]. The discrepancy could be due to a difference between real and calculated charge distributions. The inclusive Z distributions calculated in QMD+SMM for several values of κ are shown in Fig. 23 along with the experimental data. The QMD+SMM distributions are quite insensitive to κ and agree fairly well with the data. Therefore it may be possible that, on an event-by-event basis, QMD+SMM yields too many large fragments relative to the number of lighter fragments. Such charge asymmetry in the QMD+SMM emission was discussed in Ref. [11]. There it was found that smaller values of κ produce events with a larger charge asymmetry. In Fig. 22, the QMD+SMM correlation functions do show a much greater enhancement for the smaller values of κ, suggesting that the breakup pattern in nature is more symmetric than described within the QMD+SMM model.

VI. DISCUSSION AND SUMMARY

In this paper we have presented comprehensive results on two-fragment correlations for IMF's in the range $4 < Z \leq 53$ from the reactions $E/A = 50$ and 100 MeV Fe on targets of Ta, Au, and Th. The striking features of the experimental results are the presence of a Coulomb hole in the correlation functions indicative of a small time difference between the emission of the two fragments and the independence of any of the inclusive or two-particle distributions on the entrance channel. The systematics of the Coulomb hole widths, relative velocities, and other two-particle observables do not depend on the energy of the projectile or the mass of the target; small deviations can be attributed to differences in the kinematics or the mass of the target residue. Furthermore, except for effects due to conservation of mass and energy and the presence of the Coulomb hole in the two-IMF events, there are no correlations between the charge or vector velocity of the two measured fragments. In particular, there is no evidence for different types of sources contributing dominantly to different charge or angular regions in the data set. This is an indication that the multifragmentation of a large target nucleus in the energy range between $E/A = 50$ and 100 MeV is thermally driven.

A comprehensive model of these data is not currently available, but the results are compared to two complementary, limited models. Comparisons to the sequential three-body, trajectory model, MENEKA, indicate that the time scale for emission of the IMF's is < 500 fm/c in agreement with previous results involving light IMF's

[3,4,6,7]. Furthermore, given the broad charge, velocity, and angular acceptance of the PAGODA detector, our comparisons suggest that these types of correlation studies have only limited sensitivity to measure time scales below about 250 fm/c (although limitations in the early version of MENEKA used in this analysis may be responsible for the poor resolution at small values of τ [41]). At very short time scales, the distinction between sequential and simultaneous emission becomes ambiguous and a truly comprehensive theory may be necessary to go further. Comparisons to the model, QMD+SMM, indicate that a microscopic dynamical model coupled with an explosive decay of the highly excited target residue can reproduce most of the characteristics of the data. The difficulty of this approach is the *ad hoc* nature of the coupling of the two codes which is required by the failure of QMD to produce multiple fragments in the energy region near the production threshold. This result is in contrast to the success of QMD at higher energies where there is significant compression in central heavy-ion collisions. The variable in the SMM calculations is the freeze-out density parameter κ. Comparisons of the velocity correlations indicate a freeze-out volume of 3–10 times the ground state nuclear volume, but the results suggest an increase in the volume as the Coulomb product Z_1Z_2 increases.

The only significant deviations between the calculations and data are found in the pair velocity and the presence of a prominent overshoot or enhancement in the correlation functions in the region just outside the Coulomb hole. Both models show lower means for $v_{\rm pair}$ and the enhancement that is not present in the data. Whether these two effects are connected is not clear at this point, but studies of the limited three-fragment experimental data set suggests that the overshoot in the correlation function is reproduced in events where a heavy particle is formed along with the lighter observed IMF's. Such a residue is inherent in the MENEKA simulation and appears to be formed in a significant fraction of the QMD+SMM events, especially for small values of κ. The data in this experiment are not sufficient to address the question of whether a qualitative discrepancy exists with the QMD+SMM over the presence of a large target remnant.

ACKNOWLEDGMENTS

We are very grateful to Professor Walter Greiner and Professor Horst Stöcker for their continued interest and support of this project. We thank A. Botvina and I. N. Mishustin for the use of their SMM code and A. Elmaani for his assistance with MENEKA. One of us (H.C.B.) gratefully acknowledges support from the Alexander von Humbolt Foundation and the hospitality of the Institut für Theoretische Physik der Universität Frankfurt during part of this project. Three of us (M.B., T.B., and G.P.) are grateful to LLNL for hospitality and support during various times. One of us (G.P.) acknowledges support from the Wissenschaftsausschuss of NATO via the DAAD and from the Alexander von Humboldt Foundation. This work was performed under the auspices of the U.S. Department of Energy by the Lawrence Livermore National Laboratory under Contract No. W-7405-ENG-48.

[1] R. Trockel, U. Lynen, J. Pochadzalla, W. Trautmann, N. Brummund, E. Eckert, R. Glasow, K. D. Hildenbrand, K. H. Kampert, W. F. J. Müller, D. Pelte, H. J. Rabe, H. Sann, R. Santo, H. Stelzer, and R. Wada, Phys. Rev. Lett. **59**, 2844 (1987).
[2] R. Bougault, J. Colin, F. Delaunay, A. Genoux-Lubain, A. Hajfani, C. Le Brun, J. F. Lecolley, M. Louvel, and J. C. Steckmeyer, Phys. Lett. B **232**, 291 (1989).
[3] Y. D. Kim, R. T. de Souza, D. R. Bowman, N. Carlin, C. K. Gelbke, W. G. Gong, W. G. Lynch, L. Phair, M. B. Tsang, and F. Zhu, Phys. Rev. C **45**, 338 (1992); Y. D. Kim, R. T. de Souza, C. K. Gelbke, W. G. Gong, and S. Pratt, *ibid.* **45**, 387 (1992).
[4] D. Fox, R. T. de Souza, L. Phair, D. R. Bowman, N. Carlin, C. K. Gelbke, W. G. Gong, Y. D. Kim, M. A. Lisa, W. G. Lynch, G. F. Peaslee, M. B. Tsang, and F. Zhu, Phys. Rev. C **47**, R421 (1993); **48**, 3135 (1993).
[5] T. C. Sangster, M. Begemann-Blaich, Th. Blaich, H. C. Britt, A. Elmaani, N. N. Ajitanand, and M. N. Namboodiri, Phys. Rev. C **47**, R2457 (1993).
[6] D. R. Bowman, G. F. Peaslee, N. Carlin, R. T. de Souza, C. K. Gelbke, W. G. Gong, Y. D. Kim, M. A. Lisa, W. G. Lynch, L. Phair, M. B. Tsang, and C. Williams, Phys. Rev. Lett. **70**, 3534 (1993).
[7] E. Bauge, A. Elmaani, R. A. Lacey, J. Lauret, N. N. Ajitanand, D. Craig, M. Cronqvist, E. Gualtieri, S. Hannuschke, T. Li, B. Llope, T. Reposeur, A. Vander Molen, G. D. Westfall, J. S. Winfield, J. Yee, S. Yennello, A. Nadasen, R. S. Tickle, and E. Norbeck, Phys. Rev. Lett. **70**, 3705 (1993).
[8] B. Kämpfer *et al.*, Phys. Rev. C **48**, R955 (1993).
[9] T. C. Sangster, H. C. Britt, and M. N. Namboodiri, in Proceedings of the 9th High Energy Heavy Ion Study, Lawrence Berkeley Laboratory, 1993, Report No. LBL-35984, p. 25.
[10] G. Peilert, M. N. Namboodiri, T. C. Sangster, H. C. Britt, A. Botvina, and I. N. Mishustin, in *Proceedings of the XXXI Winter Meeting on Nuclear Physics*, Bormio, Italy, 1993, edited by I. Iori (Istituto di fisica dell'Universta and Istituto nationale di fisica nucleare, Milano, 1993), p. 43.
[11] G. Peilert, T. C. Sangster, M. N. Namboodiri, and H. C. Britt, J. Phys. G **20**, L105 (1994); in Proceedings of the 9th High Energy Heavy Ion Study [9], p. 74.
[12] Y. Yariv and Z. Fraenkel, Phys. Rev. C **20**, 2227 (1979); **24**, 488 (1981).
[13] V. D. Toneev and K. K. Gudima, Nucl. Phys. **A400**, 173c (1983).
[14] J. Aichelin, Phys. Rep. **202**, 233 (1991), and references therein.

[15] G. Peilert, H. Stöcker, and W. Greiner, Rep. Prog. Phys. **57**, 533 (1994).
[16] D. H. Boal and J. N. Glosli, Phys. Rev. C **37**, 91 (1988); **42**, R502 (1990).
[17] R. T. de Souza, L. Phair, D. R. Bowman, N. Carlin, C. K. Gelbke, W. G. Gong, Y. D. Kim, M. A. Lisa, W. G. Lynch, G. F. Peaslee, M. B. Tsang, H. M. Xu, F. Zhu, and W. A. Friedman, Phys. Lett. B **268**, 6 (1991).
[18] G. D. Harp, J. M. Miller, and B. J. Berne, Phys. Rev. **165**, 1166 (1968); G. D. Harp and J. M. Miller, Phys. Rev. C **3**, 1847 (1971); M. Blann, Nucl. Phys. **A235**, 211 (1974); Phys. Rev. C **31**, 295 (1985); **31**, 1245 (1985).
[19] R. J. Charity, M. A. McMahan, G. J. Wozniak, R. J. McDonald, L. G. Moretto, D. G. Sarantites, L. G. Sobotka, G. Guarino, A. Pantaleo, L. Fiore, A. Gobbi, and K. D. Hildenbrand, Nucl. Phys. **A483**, 371 (1988); D. R. Bowman, G. F. Peaslee, N. Colonna, R. J. Charity, M. A. McMahan, D. Delis, H. Han, K. Jing, G. J. Wozniak, L. G. Moretto, W. L. Kehoe, B. Libby, A. C. Mignerey, A. Moroni, S. Angius, I. Iori, A. Pantaleo, and G. Guarino, *ibid.* **A523**, 386 (1991).
[20] M. Blann and V. K. Vonach, Phys. Rev. C **28**, 1475 (1983); M. Blann, T. Komoto, and I. Tserruya, *ibid.* **40**, 2498 (1989); M. Blann, M. G. Mustafa, G. Peilert, H. Stöcker, and W. Greiner, *ibid.* **44**, 431 (1991); M. Blann and M. G. Mustafa, *ibid.* **44**, R590 (1991).
[21] A. S. Botvina, A. S. Iljinov, I. N. Mishustin, J. P. Bondorf, R. Donangelo, and K. Sneppen, Nucl. Phys. **A475**, 663 (1987); A. S. Botvina, A. S. Ijinov, and I. N. Mishustin, *ibid.* **A507**, 649 (1990).
[22] G. Fai and J. Randrup, Nucl. Phys. **A381**, 557 (1982); **A404**, 551 (1983); J. P. Bondorf, R. Donangelo, I. N. Mishustin, C. J. Pethick, H. Schulz, and K. Sneppen, *ibid.* **A443**, 321 (1985); **A444**, 460 (1985); D. H. E. Gross and X. Z. Zhang, Phys. Lett. **161B**, 47 (1985); D. Hahn and H. Stöcker, Nucl. Phys. **A476**, 718 (1988).
[23] W. A. Friedman, Phys. Rev. Lett. **60**, 2125 (1988); Phys. Rev. C **40**, 2055 (1989); **42**, 667 (1990).
[24] K. G. R. Doss, H.-A. Gustafsson, H. H. Gutbrod, J. W. Harris, B. V. Jacak, K. H. Kampert, B. Kolb, A. M. Poskanzer, H. G. Ritter, H. R. Schmidt, L. Teitelbaum, M. Ticknell, S. Weiss, and H. Wieman, Phys. Rev. Lett. **59**, 2720 (1987).
[25] T. C. Sangster, H. C. Britt, D. J. Fields, L. F. Hansen, R. G. Lanier, M. N. Namboodiri, B. A. Remington, M. L. Webb, M. Begemann-Blaich, Th. Blaich, M. M. Fowler, J. B. Wilhelmy, Y. D. Chan, A. Decal, A. Harmon, J. Pouliot, R. G. Stokstad, S. Kaufman, F. Videbaek, Z. Fraenkel, G. Peilert, H. Stöcker, W. Greiner, A. Botvina, and I. N. Mishustin, Phys. Rev. C **46**, 1404 (1992).
[26] J. P. Alard *et al.*, Phys. Rev. Lett. **69**, 889 (1992).
[27] J. Hubele, P. Kreutz, J. C. Adloff, M. Begemann-Blaich, P. Bouissou, G. Imme, I. Iori, G. J. Kumde, S. Lerav, V. Lindenstruth, Z. Lui, U. Lynen, R. J. Meier, U. Milkau, A. Moroni, W. F. J. Müller, C. Ngo, C. A. Ogilvie, J. Pochodzalla, G. Raciti, G. Rudolf, H. Sann, A. Shüttauf, W. Seidel, L. Stuttge, W. Trautmann, and A. Tucholski, Z. Phys. A **340**, 263 (1991).
[28] D. R. Bowman, G. F. Peaslee, R. T. de Souza, N. Curlin, C. K. Gelbke, W. G. Gong, Y. D. Kim, M. A. Lisa, W. G. Lynch, L. Phair, M. B. Tsang, C. Williams, N. Colonna, K. Hanhold, M. A. McMahan, G. J. Wozniak, L. G. Moretto, and W. A. Freidman, Phys. Rev. Lett. **67**, 1527 (1991).
[29] F. Saint-Laurent, M. Conjeaud, R. Dayras, S. Harar, H. Oeschler, and C. Volant, Nucl. Phys. **A422**, 307 (1984).
[30] M. Begemann-Blaich, Th. Blaich, M. M. Fowler, J. B. Wilhelmy, H. C. Britt, D. J. Fields, L. F. Hansen, R. G. Lanier, D. J. Massoletti, M. N. Namboodiri, B. A. Remington, T. C. Sangster, G. L. Struble, M. L. Webb, Y. D. Chan, A. Dacal, A. Harmon, J. Pouliot, R. G. Stokstad, S. Kaufman, F. Videbaek, and Z. Fraenkel, Phys. Rev. C **45**, 677 (1992).
[31] Th. Blaich, M. Begemann-Blaich, M. M. Fowler, J. B. Wilhelmy, H. C. Britt, D. J. Fields, L. F. Hansen, M. N. Namboodiri, T. C. Sangster, and Z. Fraenkel, Phys. Rev. C **45**, 689 (1992).
[32] H. C. Britt, D. J. Fields, L. F. Hansen, R. G. Lanier, D. J. Massoletti, M. N. Namboodiri, B. A. Remington, T. C. Sangster, G. L. Struble, M. L. Webb, M. Begemann-Blaich, Th. Blaich, M. M. Fowler, J. B. Wilhelmy, Y. D. Chan, A. Dacal, A. Harmon, J. Pouliot, R. G. Stokstad, S. B. Kaufman, F. Videbaek, and Z. Fraenkel, in *The Nuclear Equation of State*, edited by W. Greiner and H. Stöcker, Vol. 216A of *NATO Advanced Study Institute, Series B: Physics* (Plenum, New York, 1989), p. 177.
[33] C. A. Ogilvie, J. C. Adloff, M. Begemann-Blaich, P. Bouissou, J. Hubele, G. Imme, I. Iori, P. Kreutz, G. J. Kunde, S. Leray, V. Lindenstruth, Z. Liu, U. Lynen, R. J. Meijer, U. Milkau, A. Moroni, W. F. J. Müller, C. Ngo, J. Pochodzalla, G. Raciti, G. Rudolf, H. Sann, A. Schüttauf, W. Seidel, L. Stuttge, W. Trautmann, and A. Tucholski, Phys. Rev. Lett. **67**, 1214 (1991).
[34] G. Peilert, H. Stöcker, W. J. Randrup, and W. Greiner, Phys. Lett. B **260**, 271 (1991).
[35] G. F. Peaslee, M. B. Tsang, C. Schwarz, M. J. Huang, W. S. Huang, W. C. Hsi, C. Williams, W. Bauer, D. R. Bowman, M. A. Lisa, W. G. Lynch, C. M. Mader, L. Phair, J. Dinius, C. K. Gelbke, D. O. Handzy, M-C. Lemaire, S. R. Souza, G. Van Buren, R. J. Charity, L. G. Sobotka, G. J. Kunde, U. Lynen, J. Pochodzalla, H. Sann, W. Trautmann, D. Fox, R. T. de Souza, G. Peilert, W. A. Friedman, and N. Carlin, Phys. Rev. C **49**, R2271 (1994).
[36] M. B. Tsang *et al.*, Phys. Rev. Lett. **71**, 1502 (1993).
[37] M. M. Fowler, T. C. Sangster, M. L. Begemann-Blaich, T. Blaich, J. A. Boissevain, H. C. Britt, Y. D. Chan, A. Dacal, D. J. Fields, Z. Fraenkel, A. Gavron, A. Harmon, B. V. Jacak, R. G. Lanier, P. S. Lysaght, G. Mamane, D. J. Massoletti, M. N. Namboodiri, J. Pouliot, R. G. Stokstad, M. L. Webb, and J. B. Wilhelmy, Nucl. Instrum. Methods A **281**, 517 (1989).
[38] W. A. Zajc, J. A. Bistirlich, R. R. Bossingham, H. R. Bowman, C. W. Clawson, K. M. Crowe, K. A. Frankel, J. G. Ingersoll, J. M. Kurck, C. J. Martoff, D. L. Murphy, J. O. Rasmussen, J. P. Sullivan, E. Yoo, O. Hashimoto, M. Koike, W. J. McDonald, J. P. Miller, and P. Truöl, Phys. Rev. C **92**, 2173 (1984).
[39] G. I. Kopylov, Phys. Lett. **50B**, 472 (1974).
[40] A. Elmaani, N. N. Ajitanand, T. Ethvignot, and J. M. Alexander, Nucl. Instrum. Methods A **313**, 401 (1992).
[41] A. Elmaani (private communication).
[42] G. Peilert, J. Konopka, H. Stöcker, W. Greiner, M. Blann, and M. G. Mustafa, Phys. Rev. C **46**, 1457 (1992).
[43] G. Peilert, Ph.D. thesis, University of Frankfurt, 1992; GSI Report No. 92-13, ISSN 0171-4546, 1993.